DEVELOPMENTAL NEUROSCIENCE

Two phenotypically and functionally distinct microglial populations in adult zebrafish

Shuting Wu[1]*, Linh T. M. Nguyen[1]*, Hongru Pan[1], Shaoli Hassan[1], Yimei Dai[1], Jin Xu[2], Zilong Wen[1,3,4]†

Microglia are the tissue-resident macrophages in the central nervous system and are critically involved in immune defense, neural development and function, and neuroinflammation. The versatility of microglia has long been attributed to heterogeneity. Recent studies have revealed possible heterogeneity in human but not in murine microglia, yet a firm demonstration linking microglial heterogeneity to functional phenotypes remains scarce. Here, we identified two distinct microglial populations in adult zebrafish that differ in morphology, distribution, development, and function. The predominant population, phagocytotic microglia, which expresses *ccl34b.1*, is broadly distributed, amoeboid in shape, highly mobile, and phagocytotic. The other white matter–enriched *ccl34b.1*$^-$ population, regulatory microglia, has ramified protrusions but has limited mobility and phagocytosis capability. These functional differences are further supported by distinct transcriptomes and responses to bacterial infection, where *ccl34b.1*$^+$ microglia function in tissue clearance and *ccl34b.1*$^-$ microglia release immune regulators. Our study sheds light on the heterogeneity and functional diversification of microglia.

INTRODUCTION

Microglia are extraordinarily versatile immune cells in the central nervous system (CNS). As active sensor and professional phagocytes, microglia constantly surveil the environment by extending and retracting their dynamic processes (*1*, *2*). Therefore, they are highly sensitive to a variety of CNS perturbations, including pathogens, danger signals, and even neurotransmitters (*3*). Upon stimulation, microglia undergo a series of transformations from the surveillant state to the effector state, concurrently changing their morphology from ramified to amoeboid, a process termed microglial activation. This activation process can result in varied functional phenotypes, including differences in the innate immune response and interplay with the adaptive immune system, depending on the type of stimulus and physiological context (*4*). As the CNS is regarded as an "immune-privileged organ" for its delicate synaptic structures and limited regeneration capability, these immune responses need to be tightly regulated. In this regard, microglial activation can be a double-edged sword, exerting both protective and damaging effects on the CNS, which has been extensively discussed in scenarios of several neurological pathologies, such as Alzheimer's disease (*3*–*5*). Thus far, the role of microglial phagocytosis and inflammation under the pathological conditions are still controversial. Moreover, in addition to their major roles as scavengers, microglia actively participate in the patterning of the neural network, regulation of other glial cells, and vasculogenesis (*6*). How microglia balance between these flexible roles remains to be further revealed.

Because of the versatile functions that microglia exert in the CNS, it has long been proposed that they are heterogeneous populations so that different subtypes fulfill distinct functions. Several early studies indicated a possible heterogeneity of microglia across different CNS regions in terms of density, morphology, expression of several markers, and phagocytosis capability (*7*–*11*). However, recent studies, mostly in the mouse, failed to support the asserted microglial heterogeneity. Ontogenically, microglia in mouse are thought to originate from a single developmental origin—primitive hematopoietic progenitors generated in the yolk sac, which infiltrate the developing CNS during early embryogenesis and self-renew throughout the adulthood (*12*–*14*). Phenotypically, recent single-cell RNA sequencing (scRNA-seq) analysis found that adult microglia from different CNS regions form a rather homogeneous population with limited transcriptome differences, although several previously unidentified microglial subsets were identified in the embryonic and postnatal stages (*15*–*17*). In a recent cross-species scRNA-seq analysis of microglia, most examined mammals, including mouse, hamster, sheep, marmoset, and macaque, showed only one predominant microglia cell type (*18*). Nonetheless, human studies using multidimensional methods including scRNA-seq and multiplexed mass cytometry (cytometry by time of flight) of microglia in healthy human brains revealed a greater diversity (*17*, *19*, *20*). More specifically, while Böttcher *et al.* (*19*) identified several microglia subtypes that are enriched in distinct CNS regions, Sankowski *et al.* (*20*) found that microglia in the gray matter and white matter show differential expression (DE) of certain surface markers. The biological implications of these human microglia subtypes remain unknown. In summary, the heterogeneity of microglia and the regulation of microglial identity and functional phenotypes during development, homeostasis, and pathology are not fully understood.

Zebrafish microglia share a highly conserved signature genes program with their mammalian counterparts and are fully capable of responding to danger signals, clearing apoptotic neurons, and fine-tuning neuronal activity (*18*, *21*–*25*). In contrast to the single developmental origin of mouse microglia (*12*), zebrafish microglia were shown to originate from two distinct waves of hematopoiesis:

[1]Division of Life Science, State Key Laboratory of Molecular Neuroscience, Hong Kong University of Science and Technology, Clear Water Bay, Kowloon, Hong Kong, China. [2]Division of Cell, Developmental and Integrative Biology, School of Medicine, South China University of Technology, Guangdong, Guangzhou 510630, China. [3]Center of Systems Biology and Human Health, Hong Kong University of Science and Technology, Clear Water Bay, Kowloon, Hong Kong, China. [4]Greater Bay Biomedical Innocenter, Shenzhen Bay Laboratory, Shenzhen Peking University–Hong Kong University of Science and Technology Medical Center, Shenzhen 518055, China.
*These authors contributed equally to this work.
†Corresponding author. Email: zilong@ust.hk

The embryonic microglia arise from rostral blood island (RBI)–born primitive myeloid precursors and the adult microglia originate from aorta-gonad-mesonephros (AGM)–derived hematopoietic stem cells (*26*). Whether these two ontogenetically distinct populations of microglia exert specific functions during different developmental stages remains unclear, so does the heterogeneity of microglia in the homeostatic adult brain. A comparative study of microglia in zebrafish and higher vertebrates in terms of their developmental regulation, specification, and adaptation to different environmental stimulations can help to shed light on the intriguing microglia biology.

We have identified in the zebrafish brain two distinct microglial populations, phagocytotic microglia and regulatory microglia, which differ in terms of morphology, distribution pattern, origin, developmental regulation, and function. As far as we know, this is the first definitive evidence of microglia subtypes in the vertebrate adult CNS, providing fresh insights on the evolution of microglial function.

RESULTS

Two distinct microglial populations in the zebrafish brain

Previously, we have unveiled that Csf1ra (colony-stimulating factor 1 receptor a), through binding to its ligand Il34, regulates the migration and colonization of embryonic microglial precursors in zebrafish (*27*). To test whether Csf1ra signaling is also involved in the development of adult microglia, we traced the microglia phenotype in *csf1ra*-deficient fish to the juvenile stage when adult microglia begin to colonize the brain (*26*). Transverse section of the brains of wild-type (WT) and *csf1ra*$^{-/-}$ fish at 20 days postfertilization (dpf) detected a reduced but considerable number of microglia in the *csf1ra*$^{-/-}$ fish brains (Fig. 1, A and B). We noticed that the microglia in *csf1ra* mutants showed particular morphology and distribution pattern: They were highly ramified cells with complex protrusions and tended to form clusters in the central midbrain, where white matter resides (Fig. 1A). The same kind of ramified microglia could also be observed in similar brain regions of WT fish, although to a lesser extent (Fig. 1, A and B). However, there was another kind of microglia abundantly distributed in the WT brain that had amoeboid morphology with fewer protrusions, which was significantly reduced in *csf1ra*$^{-/-}$ fish (Fig. 1, A and B). Fascinated by these two morphologically and spatially distinct microglia populations, we went on to characterize them in detail in WT fish at 40 dpf and 4 months old. We found that while most microglia in the forebrain appeared to be amoeboid (fig. S1, A and B), microglia of amoeboid and ramified shape could be readily found in the midbrain and hindbrain with patterns similar to that of fish at 20 dpf, where the amoeboid microglia were broadly distributed and the ramified microglia were enriched in the white matter (Fig. 1C and fig. S1, A and B). While the amoeboid microglia dominate in number in all stages, the ratio of ramified microglia slightly increased as the fish grew older and reached approximately 20% of total microglia per midbrain slice in the adult stage (Fig. 1, C and D). These results indicate that there are two microglial populations in the zebrafish brains throughout juvenile and adult stages, and they differ not only in morphology and distribution patterns but also in their dependency on Csf1ra signaling.

To examine whether these two populations represent simply different states of the microglia (e.g., activated or resting) or two ontogenically distinct subtypes, we asked whether they develop separately during embryogenesis. Microglia in zebrafish are derived from two distinct origins (*26*). Embryonic microglia originate exclusively from primitive macrophages generated in the RBI region, but they are gradually replaced by the second wave of microglia, which arise from definitive hematopoietic cells generated in the AGM region (*26*). We first tested whether these different waves of hematopoiesis contribute differentially to the two microglial populations by temporal-spatial resolution fate mapping with the IR-LEGO-CreER-loxP cell labeling system (Fig. 1E) (*26*). To label most RBI- or AGM-derived macrophages, we heat-shocked the entire respective region in *Tg(hsp70:mCherry-T2a-CreERT2;mpeg1:loxP-DsRedx-loxP-GFP)* double transgenic embryos and analyzed at 1 month (Fig. 1F). We found that while both RBI and AGM irradiation labeled widely distributed amoeboid cells, only AGM irradiation could label white matter–enriched ramified cells (Fig. 1F). This indicates that the amoeboid microglia arise from both the RBI and the AGM and the ramified cells, on the contrary, are exclusively derived from the AGM. To further dissect their developmental origins, we heat-shocked a single tiny spot in the AGM region of embryos and analyzed at 1 month in searching for lineage-biased labeling patterns. Fish with only widely distributed amoeboid cells or white matter–enriched ramified cells being labeled were detected (Fig. 1G), suggesting that amoeboid and ramified microglia develop independently. In summary, we have identified two distinct microglial populations in juvenile and adult zebrafish that differ in their morphology, distribution, Csf1r signaling dependency, and developmental origin.

Identification of *ccl34b.1* as a microglial subtype–specific marker

In searching for a subtype-specific marker that can potentially distinguish these two microglial subpopulations, we performed in situ hybridization in the adult brain slice of candidate genes that were demonstrated to be highly expressed in microglia in our previous RNA-seq analysis. One of these candidates, chemokine (C-C motif) ligand 34b, duplicate 1 (*ccl34b.1*), showed a strong expression pattern in only a part of the microglia in the midbrain, most of which had an amoeboid morphology (Fig. 2A), suggesting that *ccl34b.1* is enriched in amoeboid microglia. To support this notion, we examined the expression of *ccl34b.1* at early embryonic stages, when the embryos contain exclusively RBI-derived amoeboid microglia (Fig. 1F). *ccl34b.1* was strongly expressed in all brain and retina microglia at 3 dpf and in some mature macrophages throughout the body (fig. S2, A and B). Thus, *ccl34b.1* holds a strong potential to serve as a specific marker for the amoeboid microglia.

To better characterize the two microglial subpopulations, we generated the *TgBAC(ccl34b.1:eGFP)* reporter line through bacterial artificial chromosome (BAC) transgenesis, replacing most of the coding region of *ccl34b.1* with an enhanced green fluorescent protein (eGFP) reporter (fig. S2C). By crossing *TgBAC(ccl34b.1:eGFP)* with *Tg(mpeg1:DsRedx),* a macrophage reporter line (*28*), we verified that the *TgBAC(ccl34b.1:eGFP)* reporter line authentically recaptures the expression pattern of endogenous *ccl34b.1* at 3 dpf, in all CNS microglia and partial peripheral mature macrophages (fig. S2D). In the brain of 1-, 2-, and 3-month-old *TgBAC(ccl34b.1:eGFP)* fish, amoeboid GFP signal could be readily detected throughout the CNS, including the brain, retina, and spinal cord (Fig. 2B and fig. S2, E and F). In addition to these GFP^{+} microglia, a small group of GFP^{-} microglia, which coexpress panleukocyte marker Lcp1 or panmacrophage marker *mpeg1*, was consistently found in the white matter regions where ramified microglia resided, and their number also accorded with our previous quantification of ramified microglia

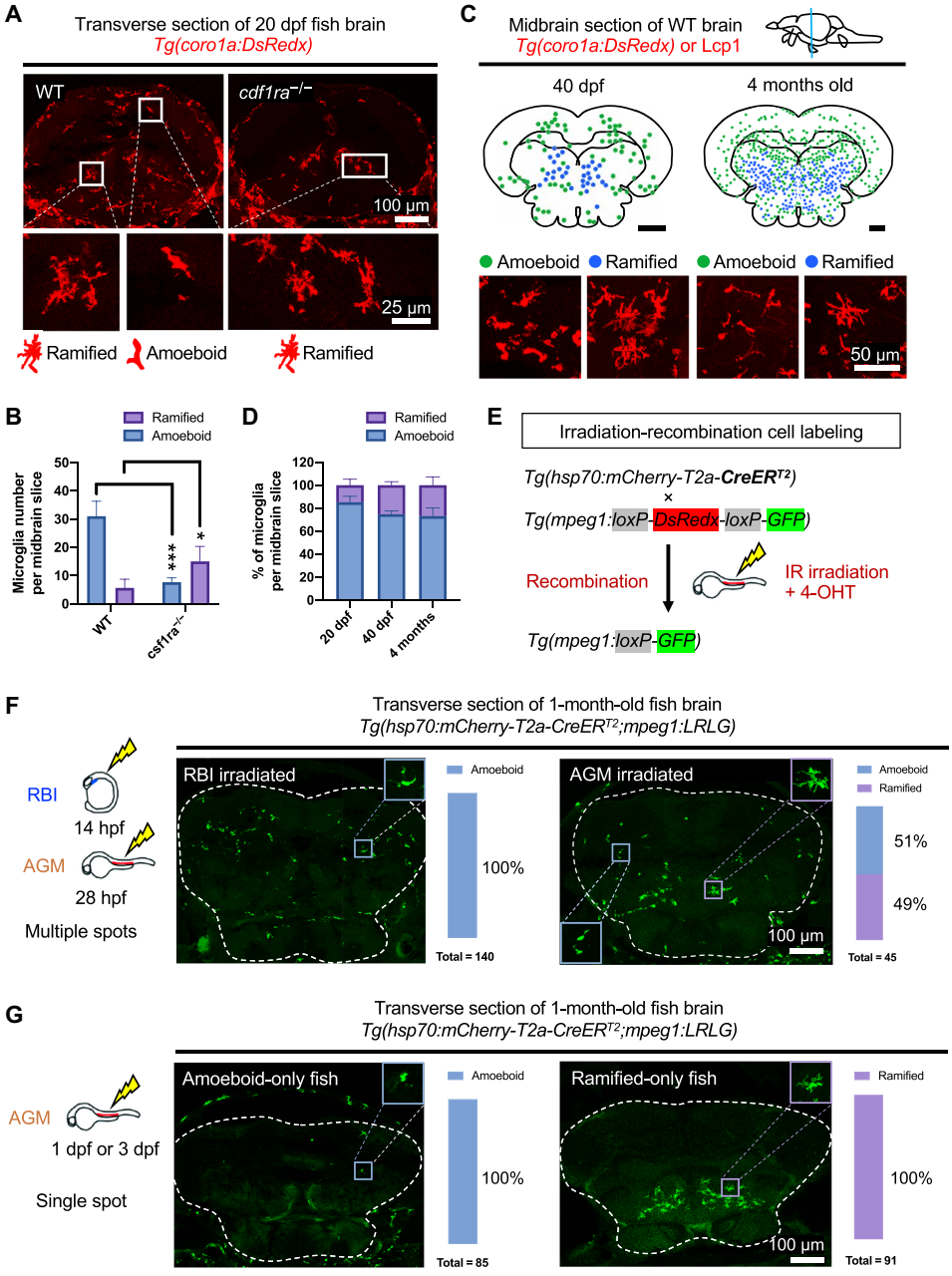

Fig. 1. Characterization of the two microglial populations in zebrafish. (**A**) Midbrain transverse sections of 20 dpf WT or *csf1ra*$^{-/-}$ fish. Microglia of amoeboid or ramified shapes are enlarged in the bottom panel. (**B**) Quantification of amoeboid or ramified microglia in the midbrain transverse sections of 20 dpf *Tg(coro1a:DsRedx)* WT or *csf1ra*$^{-/-}$ fish ($n = 3$). (**C**) Top: The number and distribution pattern of amoeboid (green dots) or ramified microglia (blue dots) in the midbrain transverse sections of 40 dpf or 4-month-old WT fish. Scale bars, 200 μm. Bottom: Enlarged images of representative amoeboid or ramified microglia. See also fig. S1 (A and B). (**D**) Quantification of the relative ratio of amoeboid or ramified microglia in the midbrain transverse sections of 20 dpf, 40 dpf, and 4-month-old WT fish ($n = 3$). (**E**) The IR-LEGO-CreER-loxP cell labeling system (*26*). IR, infrared. 4-OHT, 4-Hydroxytamoxifen. (**F** and **G**) Left: The irradiation scheme. RBI irradiation, $n = 8$; AGM irradiation, $n = 3$. hpf, hours postfertilization. Right: Representative images of microglia labeled by green fluorescent protein (GFP) in the transverse brain section of 1-month-old irradiated fish, with the brain indicated by dashed lines and representative amoeboid or ramified microglia enlarged in the corner. Bar graphs show the quantification of the relative ratio of GFP$^+$ amoeboid or ramified microglia in each fish. *$P \leq 0.05$; ***$P \leq 0.001$.

(Fig. 2, B to D). Unlike the widely distributed GFP$^+$ microglia, GFP$^-$ microglia were abundant in the central midbrain and ventral hindbrain, fewer in number in the forebrain and spinal cord, and undetectable in the retina (Fig. 2D and fig. S2, E and F). While GFP$^+$ microglia exhibited large cell bodies with few thin protrusions, GFP$^-$ microglia, on the contrary, had indistinguishable cell bodies and highly ramified protrusions (Fig. 2E). Last, when we crossed the *TgBAC(ccl34b.1:eGFP)* reporter line with *csf1ra*$^{-/-}$ fish to check the dependency of these two microglia populations on Csf1ra signaling, we found that the density of GFP$^+$ microglia, but not GFP$^-$ microglia, was significantly decreased in *csf1ra* mutants (Fig. 2, F and G). On the basis of the developmental dynamics, distribution pattern,

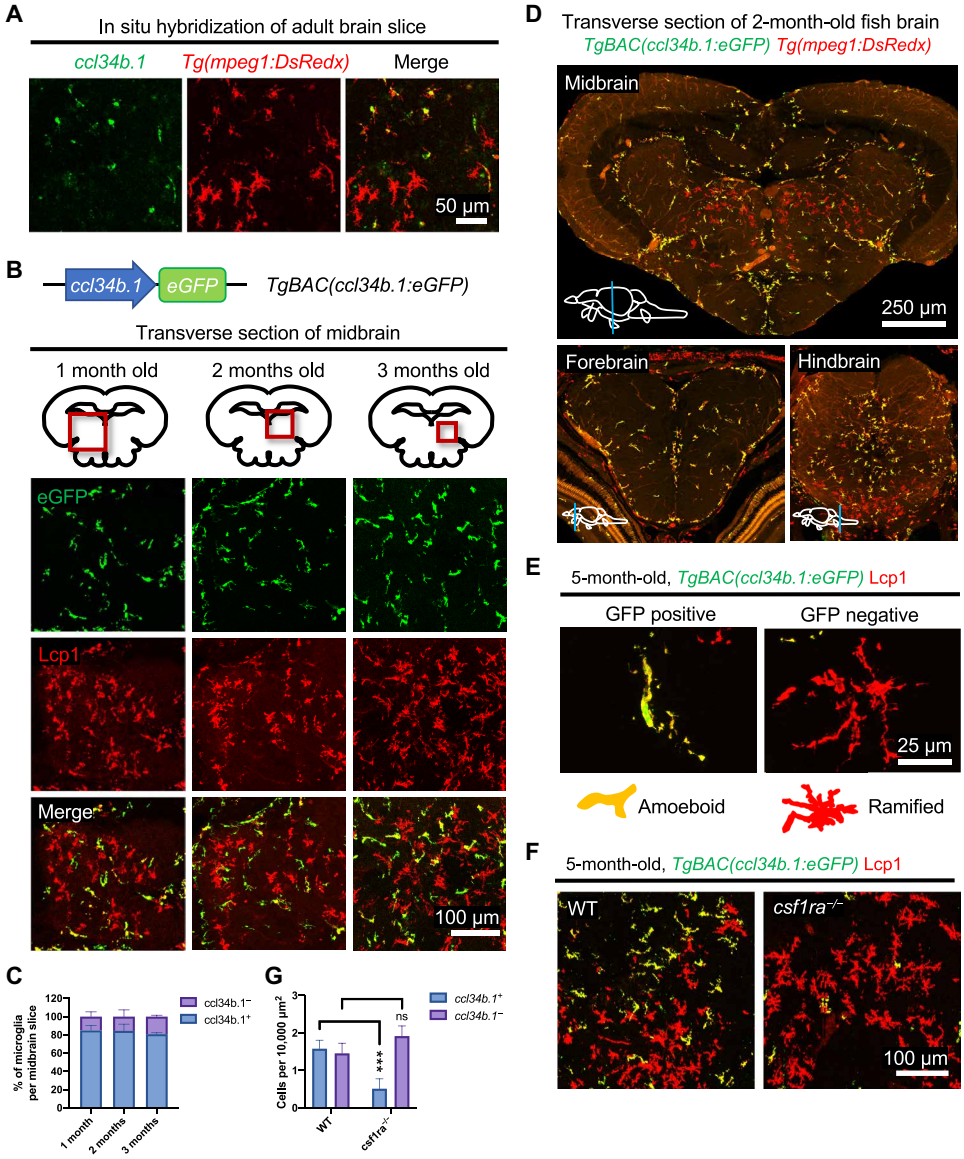

Fig. 2. Characterization of the *TgBAC(ccl34b.1:eGFP)* reporter line. (**A**) In situ hybridization and immunostaining showing *ccl34b.1* expression (green) and macrophages/microglia (red) in transverse brain sections of 3-month-old *Tg(mpeg1:DsRedx)* fish. (**B**) Top: The *TgBAC(ccl34b.1:eGFP)* reporter line. Bottom: Representative transverse sections through the midbrains of 1-, 2-, and 3-month-old *TgBAC(ccl34b.1:eGFP)* fish, respectively. *ccl34b.1*$^+$ microglia were labeled in green, and macrophage/microglia were labeled by Lcp1 (red). Exact locations of the imaging area are indicated by red boxes in the midbrain diagrams. (**C**) Quantification of relative ratio of *ccl34b.1*$^+$Lcp1$^+$ and *ccl34b.1*$^-$Lcp1$^+$ microglia in the midbrain transverse sections of 1-, 2-, and 3-month-old *TgBAC(ccl34b.1:eGFP)* fish, respectively ($n = 3$). (**D**) Transverse sections through the midbrain, forebrain, and hindbrain of 2-month-old *TgBAC(ccl34b.1:eGFP);Tg(mpeg1:DsRedx)* fish. (**E**) Representative images of amoeboid *ccl34b.1*$^+$Lcp1$^+$ and ramified *ccl34b.1*$^-$Lcp1$^+$ microglia in the transverse brain sections of 5-month-old *TgBAC(ccl34b.1:eGFP)* fish. (**F** and **G**) Representative images (F) and quantification of the density (G) of *ccl34b.1*$^+$Lcp1$^+$ and *ccl34b.1*$^-$Lcp1$^+$ microglia in the midbrain transverse sections of 5-month-old *TgBAC(ccl34b.1:eGFP)* WT or *csf1ra*$^{-/-}$ fish ($n = 4$). ns, not significant. ***$P \leq 0.001$.

morphology, and Csf1ra dependency, we concluded that we have successfully established a *TgBAC(ccl34b.1:eGFP)* reporter line that specifically labels amoeboid microglia in the CNS, providing a useful tool to further characterize these two microglial subpopulations.

Transcriptome profiling of microglial subpopulations

With the amoeboid microglia–specific *TgBAC(ccl34b.1:eGFP)* reporter line and the panmicroglia *Tg(mpeg1:DsRedx)* reporter line, we are now able to characterize these two microglial populations through fluorescence-activated cell sorting (FACS). FACS analysis of whole brains of 4-month-old *TgBAC(ccl34b.1:eGFP);Tg(mpeg1:DsRedx)* double transgenic fish showed that ~77% of brain *mpeg1*$^+$ cells were *ccl34b.1*$^+$ (GFP$^+$DsRedx$^+$ population) and ~23% were *ccl34b.1*$^-$ (GFP$^-$DsRed$^+$ population) (Fig. 3A). We then sorted the *ccl34b.1*$^+$ and *ccl34b.1*$^-$ microglia from five 4-month-old double transgenic fish and performed whole-transcriptome RNA-seq (Fig. 3A). To gain a general overview of their cell identities, we first compared their transcriptome profiles with the profiles of Langerhans cells (the tissue-resident macrophages in the epidermis), T cells, and neutrophils from our previous studies (*29*). The principal components

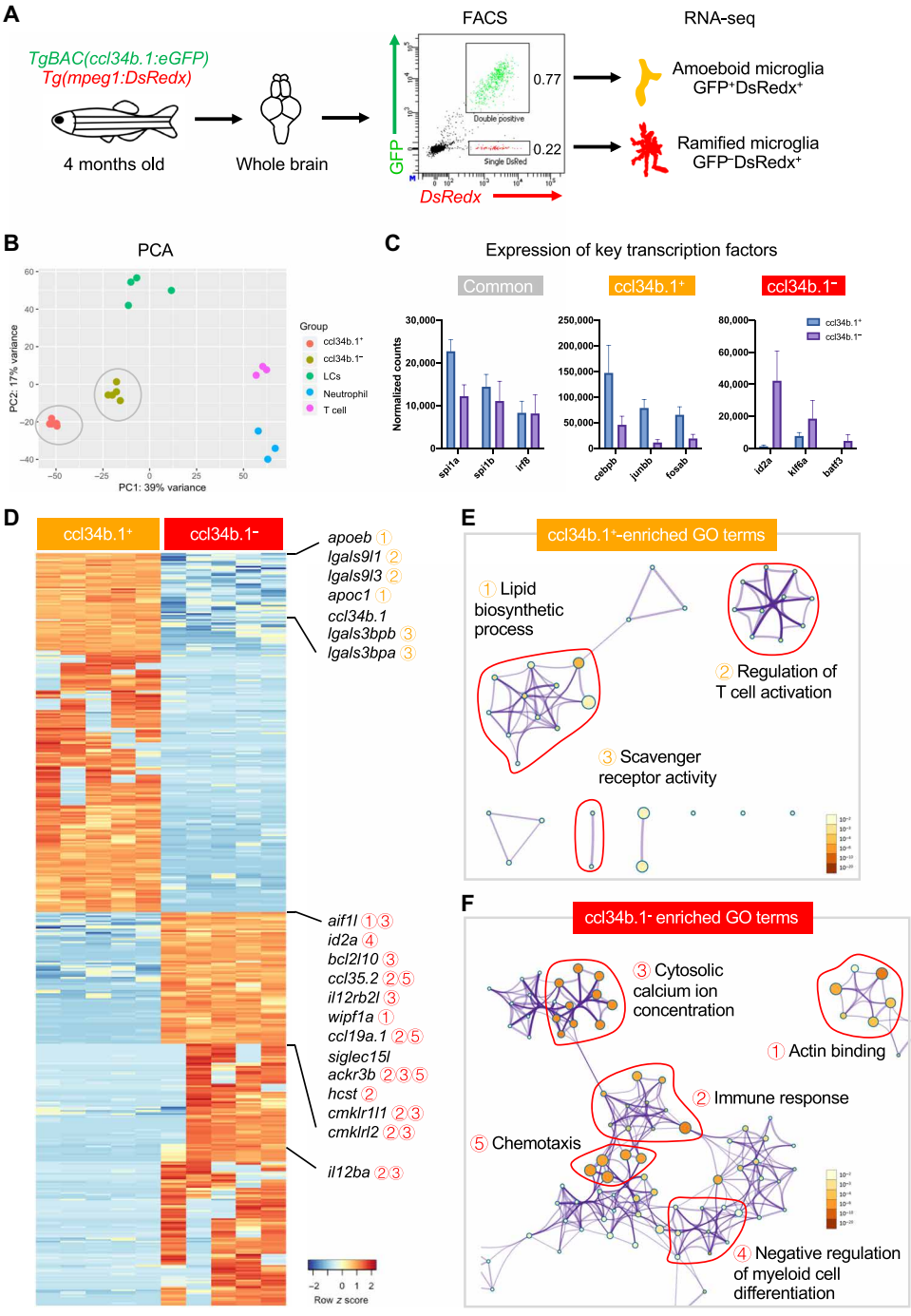

Fig. 3. Transcriptome profiling of the two microglial populations. (**A**) Experimental design of transcriptome profiling. *ccl34b.1*$^{+}$*mpeg1*$^{+}$ (amoeboid) and *ccl34b.1*$^{-}$*mpeg1*$^{+}$ (ramified) microglia were sorted from the brains of 4-month-old *TgBAC(ccl34b.1:eGFP);Tg(mpeg1:DsRedx)* fish and processed to RNA-seq ($n = 5$). (**B**) PCA plot of *ccl34b.1*$^{+}$ microglia ($n = 5$) and *ccl34b.1*$^{-}$ microglia ($n = 5$) from this study and Langerhans cells (LCs) ($n = 4$), epidermic neutrophils ($n = 3$), and epidermic T cells ($n = 3$) from a previous study (*29*). Clusters of the two microglial populations were circled in gray. (**C**) Normalized expression of several key transcription factors highly enriched in the *ccl34b.1*$^{+}$ and *ccl34b.1*$^{-}$ microglia. (**D**) Heatmap showing the relative expression of 465 selected DE genes in *ccl34b.1*$^{+}$ and *ccl34b.1*$^{-}$ microglia, with several genes highlighted in the legends. The number after the genes indicates their GO term category marked in (E) and (F). (**E** and **F**) Metascape network plots showing the relationship of the enriched GO terms in the 345 *ccl34b.1*$^{+}$ microglia–enriched DE genes (E) or the 340 *ccl34b.1*$^{-}$ microglia–enriched DE genes (F). The size of each dot indicates the number of DE genes identified for specific GO terms, and the color indicates the *P* value. The top-ranking GO terms were circled in red and highlighted. *$P \leq 0.05$; ****$P \leq 0.0001$.

analysis (PCA) showed that the *ccl34b.1*$^+$ and *ccl34b.1*$^-$ microglia formed two distinct clusters separated from other myeloid and lymphoid populations (Fig. 3B). To further analyze their common features as macrophages, we performed DE gene analysis of both microglial populations versus T cells, respectively (fig. S3A). Comparison of the enriched genes in the *ccl34b.1*$^+$ microglia and *ccl34b.1*$^-$ microglia showed a moderate overlapping pattern, with 39% of *ccl34b.1*$^+$ DE genes and 60% of *ccl34b.1*$^-$ DE genes being shared (fig. S3A). Gene ontology (GO) term analysis revealed an enrichment of immune-related terms in both populations, including immune response (GO:0006955), cell migration (GO:0016477), cell chemotaxis (GO:0060326), response to biotic stimulus (GO:0009607), and regulation of immune system process (GO:0002682) (fig. S3B). These results indicate that they are both immune-competent macrophages in the CNS.

Consistent with the common macrophage features shared by the two microglial populations, we noticed that both populations expressed considerable levels of several key myeloid transcription factors, namely, *spi1a*, *spi1b*, and *irf8* (Fig. 3C). They also highly expressed respective transcription factors, such as *cebpb*, *junbb*, and *fosab* for *ccl34b.1*$^+$ microglia and *id2a*, *klf6a*, and *batf3* for *ccl34b.1*$^-$ microglia, which might shape their individual cellular identities (Fig. 3C). To better compare their functional differences, we directly performed DE gene analysis between them (Fig. 3D). We identified a total of 685 DE genes, with 345 genes enriched in the *ccl34b.1*$^+$ population and 340 genes enriched in the *ccl34b.1*$^-$ population (Fig. 3D). Top-ranking GO terms enriched in the *ccl34b.1*$^+$ microglia–DE genes were lipid biosynthetic process (GO:0008610, e.g., *apoc1* and *apoeb*), regulation of T cell activation (GO:0050863, e.g., *lgals9l1*and *lgals9l3*), and scavenger receptor activity (GO:0005044, e.g., *lgals3bpb* and *lgals3bpa*) (Fig. 3, D and E). While scavenger receptors serve as a major part of innate pattern recognition receptors, active lipid biosynthesis is required for membrane reorganization and generation of several inflammatory mediators during macrophage activation, indicating that the *ccl34b.1*$^+$ microglia may be in an immune alarm state directly involving in phagocytosis and inflammation. For the genes enriched in the *ccl34b.1*$^-$ population, top-ranking GO terms include actin binding (GO:0003779, e.g., *aif1l* and *wipf1a*), immune response (GO:0006955, e.g., *ccl19a.1* and *ccl35.2*), regulation of cytosolic calcium ion concentration (GO:0051480, e.g., *bcl2l10* and *il12rb2l*), negative regulation of myeloid cell differentiation (GO:0045638, e.g., *id2a*), and chemotaxis (GO:0006935, e.g., *ccl19a.1* and *ccl35.2*) (Fig. 3, D and F). Notably, most of the DE genes enriched in the term immune response term (GO:0006955) and the term regulation of cytosolic calcium ion concentration (GO:0051480) are chemokines, cytokines, receptors, and signaling adaptors, such as *ccl19a.1*, *ccl35.2*, *il12ba*, *cmklrl2*, *cmklr1l1*, *ackr3b*, *il12rb2l*, and *hcst* (Fig. 3D). Therefore, we speculated that the *ccl34b.1*$^-$ microglia population actively responds to and regulates the CNS microenvironment through chemokine and cytokine signaling, resulting in the changes of cytosolic calcium ion concentration, cytoskeleton organization, cell motility, and the release of immune regulators. In summary, transcriptome profiling indicates that these two microglial populations are functionally diverse and may contribute synergistically to the CNS homeostasis.

Distinct behavior and phagocytosis capability of microglial subpopulations

Transcriptome profiling of the *ccl34b.1*$^+$ and the *ccl34b.1*$^-$ microglial populations indicates that they both undergo active cytoskeleton remodeling and might be highly mobile (Fig. 3, E and F). To catch a glimpse of their behavioral dynamics, we performed time-lapse confocal imaging of microglia in acute brain slice cultures of *TgBAC(ccl34b.1:eGFP);Tg(mpeg1:DsRedx)* double transgenic fish (Fig. 4A). During the 12-hour imaging period, the brain slice survived well with a possible activation phenotype of *ccl34b.1*$^+$ or *ccl34b.1*$^-$ microglia (movie S1). Notably, the two microglial populations exhibited distinct behavioral dynamics (movie S1). The *ccl34b.1*$^+$ microglia moved actively by sending a major pseudopod and retraction of a long uropod, a characteristic pattern of amoeboid cell movement [Fig. 4, B (cell 1) and C]. The *ccl34b.1*$^-$ microglia, on the contrary, remained ramified and stayed in the same location during the whole imaging period, only extending and retracting their multiple protrusions [Fig. 4, B (cell 2) and C]. This result indicates that, while the *ccl34b.1*$^+$ microglia can migrate actively through amoeboid movement in response to stimuli (such as injury in this case), the *ccl34b.1*$^-$ microglia remain immobile, and they possibly regulate their neighboring cells and the CNS environment through direct contact or secreted molecules. The DE genes related to actin binding and cell mobility in the *ccl34b.1*$^-$ microglia are, therefore, likely required for the dynamic changes of their ramified protrusions.

To assay the phagocytosis capability of the two microglial populations, we incubated the brain slice with pHrodo *Escherichia coli* BioParticles Conjugate, whose fluorescence increases in the acidic lysosomal environment after being phagocytosed. We first incubated the brain slice of *TgBAC(ccl34b.1:eGFP)* fish with pHrodo Red *E. coli* BioParticles Conjugate. In time-lapse imaging, *ccl34b.1*$^+$ microglia actively phagocytosed the pHrodo Red BioParticles, became round, and started emitting bright red fluorescence (Fig. 4D). At 4 hours posttreatment, approximately 20% of *ccl34b.1*$^+$ microglia were pHrodo red positive (Fig. 4, D and E). The phagocytosis capability of *ccl34b.1*$^+$ microglia might be underestimated in this assay since the microglia in the deep tissue are not accessible to the particles in the culture medium. When we incubated the freshly prepared whole-brain cell suspension of *TgBAC(ccl34b.1:eGFP)* fish with pHrodo Red *E. coli* BioParticles Conjugate and assayed their red fluorescence through FACS, 86.5% of *ccl34b.1*$^+$ microglia were pHrodo red positive after 1-hour incubation (fig. S4). These experiments showed that the *ccl34b.1*$^+$ microglia are highly phagocytotic. Notably, in the brain slice of *TgBAC(ccl34b.1:eGFP)* fish incubated with pHrodo Red *E. coli* BioParticles, all bright red signal colocalized with eGFP signal, indicating that the *ccl34b.1*$^+$ microglia were the only phagocytotic cells responding to *E. coli* bioparticles in the brain (Fig. 4D). It was, therefore, not unexpected that when we incubated the brain slice of *TgBAC(ccl34b.1:eGFP);Tg(mpeg1:DsRedx)* fish with pHrodo Green *E. coli* BioParticles Conjugate, we found that *ccl34b.1*$^-$ microglia did not ingest any pHrodo Green *E. coli* BioParticles that emitted green fluorescence in the whole 12-hour imaging period (Fig. 4F). This indicates that the *ccl34b.1*$^-$ microglia have low phagocytosis capability of *E. coli* bioparticle. Collectively, the acute brain slice culture imaging and *E. coli* bioparticle phagocytosis assay reveal distinct behavioral dynamics and phagocytosis capability of the two microglial populations.

Distinct responses to bacterial infection of microglial subpopulations

To better understand the physiological function of the two microglia populations in immune defense processes, we established a CNS bacterial infection model. Live *E. coli* or phosphate-buffered saline (PBS),

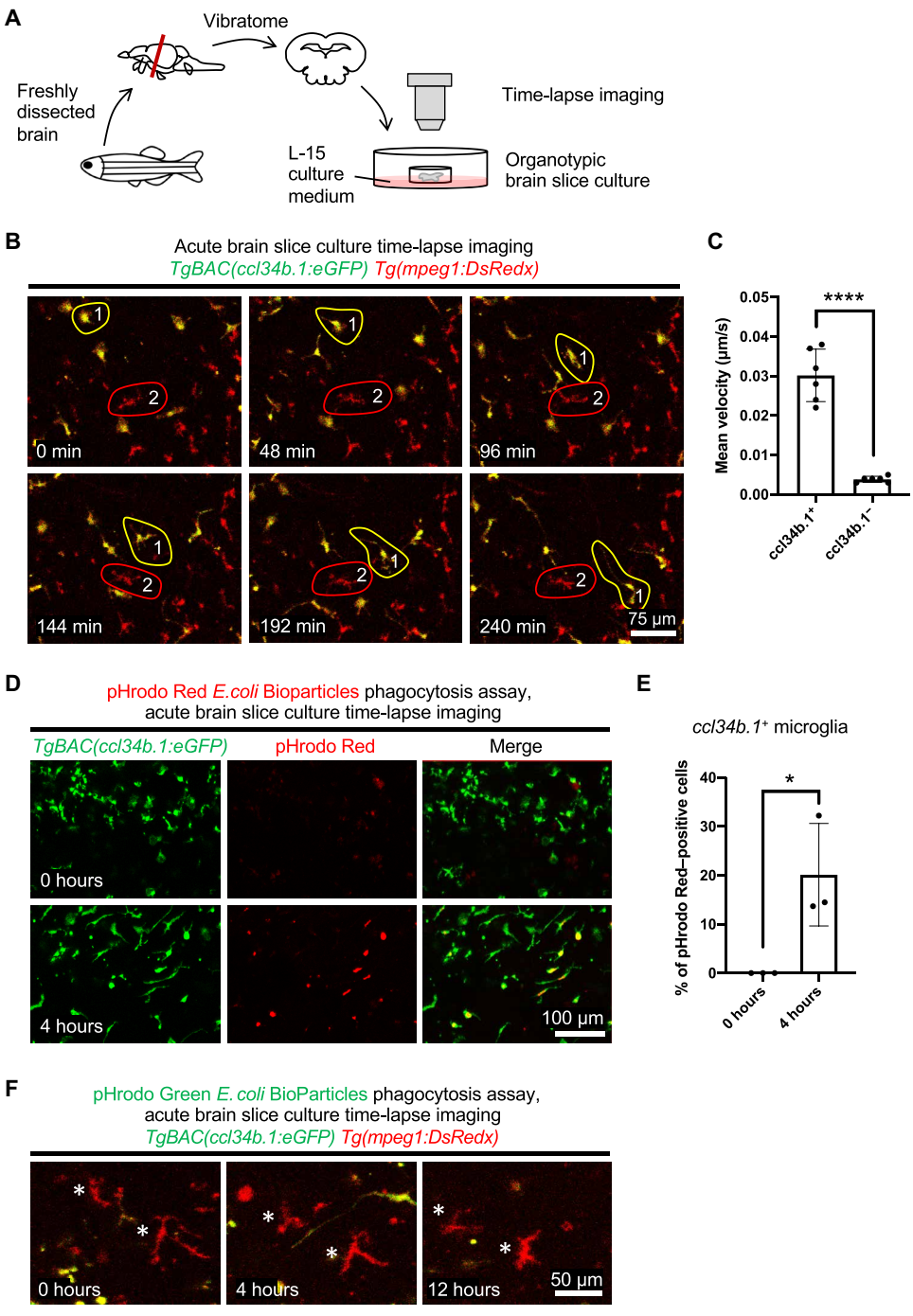

Fig. 4. Acute brain slice culture of the two microglial populations. (**A**) Experimental design of the acute brain slice culture. Brains were freshly dissected and applied to vibratome sectioning, with a thickness of 200 μm. Slices were then cultured in an imaging chamber with L-15 medium [10% fetal bovine serum (FBS)] and monitored under a confocal microscope. (**B**) Representative frames from the time-lapse imaging of a typical midbrain slice of *TgBAC(ccl34b.1:eGFP);Tg(mpeg1:DsRedx)* fish showing the dynamic behavior of *ccl34b.1*$^{+}$ microglia (yellow) and *ccl34b.1*$^{-}$ microglia (red). Examples of the cell movement (cell 1 and cell 2) were circled for the respective group. (**C**) Quantification of the mean velocity of *ccl34b.1*$^{+}$ and *ccl34b.1*$^{-}$ microglia in the time-lapse imaging of midbrain slice of *TgBAC(ccl34b.1:eGFP);Tg(mpeg1:DsRedx)* fish ($n = 6$). (**D**) Representative frames from the time-lapse imaging of midbrain slice of the *TgBAC(ccl34b.1:eGFP)* fish incubated with pHrodo Red *E. coli* BioParticles showing the uptake of red particles by *ccl34b.1*$^{+}$ microglia (green) after 4 hours. (**E**) Quantification of the percentage of *ccl34b.1*$^{+}$ microglia containing the pHrodo Red *E. coli* BioParticles after a 4-hour incubation ($n = 3$). (**F**) Representative frames from the time-lapse imaging of midbrain slice of *TgBAC(ccl34b.1:eGFP);Tg(mpeg1:DsRedx)* fish incubated with pHrodo Green *E. coli* BioParticles, showing that *ccl34b.1*$^{-}$ microglia (red, asterisk) did not intake any green particles after 12 hours. *$P \leq 0.05$; ****$P \leq 0.0001$.

together with the fluorescent indicator Alexa Fluor 647 dye, was injected into the cerebroventricles of 4-month-old *TgBAC(ccl34b.1:eGFP); Tg(mpeg1:DsRedx)* double transgenic fish, and the fish were then euthanized at 6 hours postinjection (hpi) and subjected to brain cryo-section and immunostaining (Fig. 5A). In the transverse brain section of the *E. coli*–injected fish, we observed a marked response of the *ccl34b.1*$^+$ microglia throughout the brain (Fig. 5B and fig. S5). Instead of being evenly distributed in different brain regions, the *ccl34b.1*$^+$ microglia in the *E. coli*–injected fish accumulated in the injection site and in the subventricular zone of all brain ventricles, including the forebrain ventricle, the tectal ventricle, the third ventricle, and the fourth ventricle, indicating that the *E. coli*–induced inflammatory signal spread out through the ventricular system (Fig. 5B and fig. S5). These subventricular *ccl34b.1*$^+$ microglia were swollen in morphology and formed clusters, indicating that they were activated and probably phagocytosing the *E. coli* in the ventricles (Fig. 5B and fig. S5). Accordingly, their density in the parenchyma decreased significantly when compared with those in the WT or PBS-injected fish (Fig. 5, B and C, and fig. S5). On the contrary, the distribution of the *ccl34b.1*$^-$ microglia remained unchanged, so did their density in the parenchyma (Fig. 5, B and C, and fig. S5). These observations are highly consistent with the distinct behavioral dynamics revealed from acute brain slice culture (Fig. 4). Therefore, we reasoned that the highly mobile and phagocytotic *ccl34b.1*$^+$ microglia play major roles in tissue clearing upon bacterial infection, while the less mobile *ccl34b.1*$^-$ microglia might regulate inflammation indirectly.

Transcriptome profiling of bacteria-challenged microglial subpopulations

To better characterize the respective functions of *ccl34b.1*$^+$ and *ccl34b.1*$^-$ microglia at the molecular level during bacterial infection and acute inflammation, we isolated microglia from 6-month-old WT, PBS-injected, and *E. coli*–injected fish at 6 hpi and performed transcriptome profiling (Fig. 6A). Both microglial populations responded to *E. coli*. PCA results showed that the *ccl34b.1*$^+$ and the *ccl34b.1*$^-$ microglia in the *E. coli*–injected fish formed two distinct clusters, distinct from each other and also well separated from their respective WT and PBS-injected fish controls (Fig. 6B). The *ccl34b.1*$^+$ microglia exhibited a farther intergroup distance than the *ccl34b.1*$^-$ microglia, indicating that their transcriptome changes were more significant (Fig. 6B). DE gene analysis of *ccl34b.1*$^+$ microglia in *E. coli*–injected fish versus PBS-injected fish revealed a total of 562 DE genes (177 up-regulated and 385 down-regulated) (Fig. 6C), while 334 DE genes (59 up-regulated and 275 down-regulated) were identified for the *ccl34b.1*$^-$ microglia in *E. coli*–injected fish versus PBS-injected fish (Fig. 6D). We then focused on the up-regulated genes in the *E. coli*–challenged groups in our subsequent analysis. Notably, the genes up-regulated in the two *E. coli*–challenged groups (*ccl34b.1*$^+$ microglia and *ccl34b.1*$^-$ microglia) exhibited a largely nonoverlapping pattern, and GO term enrichment analysis revealed both shared and unique GO terms, suggesting that the upregulated genes might play divergent roles in these two groups of microglia (Fig. 6, E and F). In the *E. coli*–challenged *ccl34b.1*$^+$ microglia, significantly up-regulated genes include proinflammatory cytokines

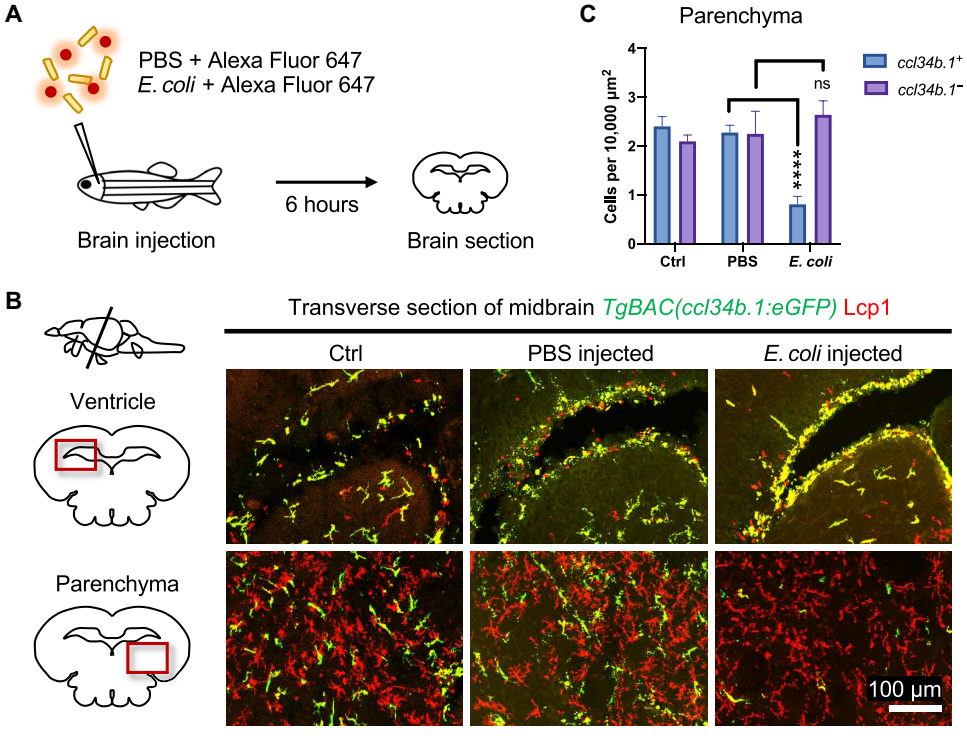

Fig. 5. Responses of the two microglial populations to CNS bacterial infection. (**A**) Experimental design. *E. coli* or PBS was coinjected with the Alexa Fluor 647 dye into the cerebroventricles of 4-month-old *TgBAC(ccl34b.1:eGFP)* fish, and their brains are collected for cryo-section after 6 hours. (**B**) Transverse midbrain sections of WT, PBS-injected, and *E. coli*–injected 4-month-old *TgBAC(ccl34b.1:eGFP)* fish, with the *ccl34b.1*$^+$ microglia labeled in green/yellow and the *ccl34b.1*$^-$ microglia labeled in red. Exact locations of the imaging area are indicated by red boxes in the midbrain diagrams. (**C**) Quantification of density of *ccl34b.1*$^+$ and *ccl34b.1*$^-$ microglia in the midbrain parenchyma of WT fish ($n = 3$), PBS-injected fish ($n = 6$), and *E. coli*–injected fish ($n = 6$).

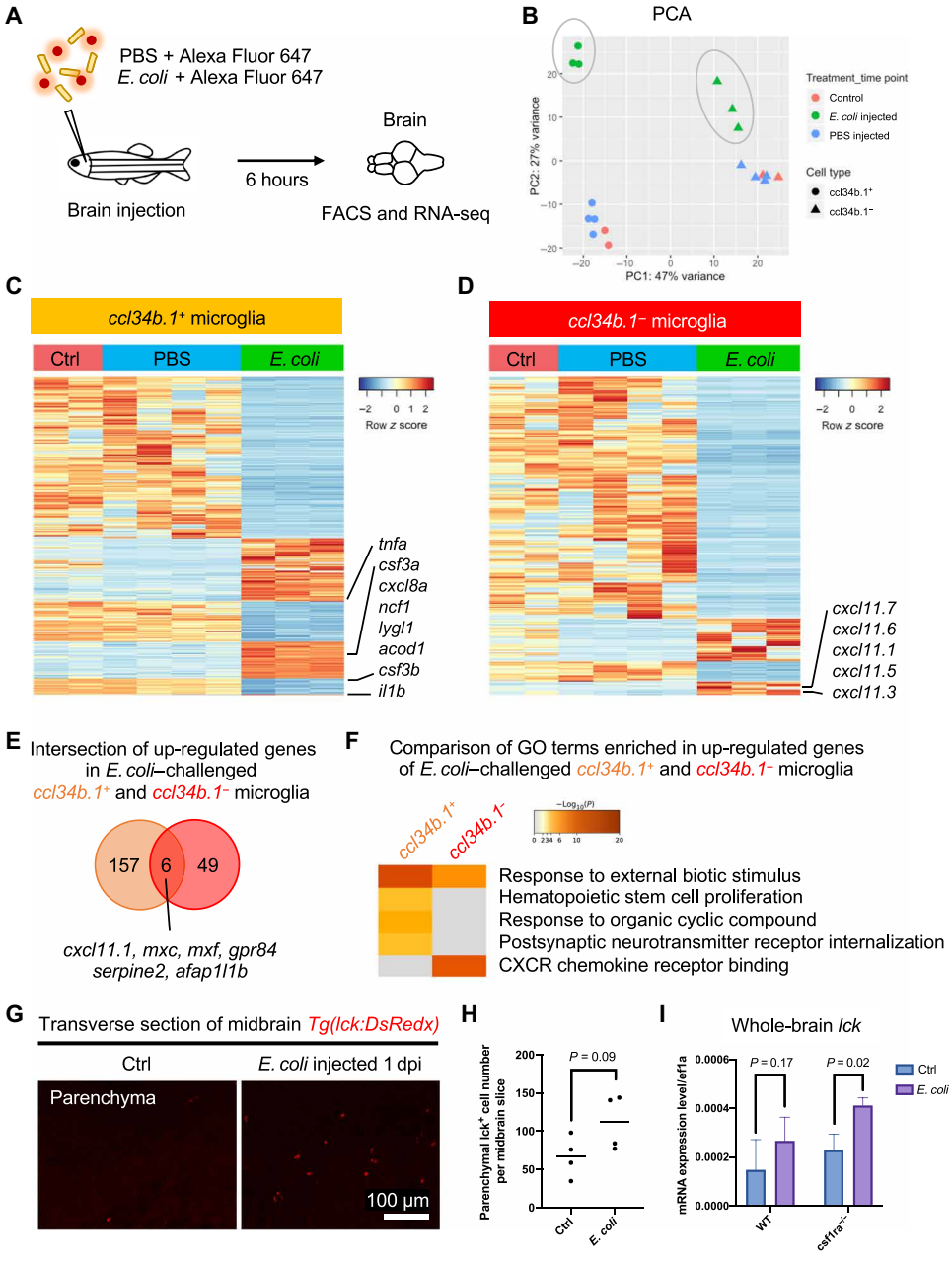

Fig. 6. Transcriptome profiling of the two microglial populations to bacterial infection. (**A**) Experimental design. *E. coli* or PBS was coinjected with the Alexa Fluor 647 dye into the cerebroventricles of 6-month-old *TgBAC(ccl34b.1:eGFP);Tg(mpeg1:DsRedx)* fish, and brains are collected for FACS and RNA-seq after 6 hours. (**B**) PCA plot of *ccl34b.1*$^{+}$ and *ccl34b.1*$^{−}$ microglia from WT ($n = 2$), PBS-injected ($n = 4$), and *E. coli*–injected ($n = 3$) fish. Clusters of the two microglial populations from the *E. coli*–injected fish are circled in gray. (**C** and **D**) Heatmap showing the relative expression of DE genes of *E. coli*–challenged *ccl34b.1*$^{+}$ microglia (C) and *ccl34b.1*$^{−}$ microglia (D) versus PBS-injected groups, with several genes highlighted. (**E**) Diagram showing the intersection of up-regulated genes in *E. coli*–challenged *ccl34b.1*$^{+}$ and *ccl34b.1*$^{−}$ microglia. The shared six genes are listed. (**F**) Metascape heatmap showing the top five enriched GO terms of the up-regulated genes in *E. coli*–challenged *ccl34b.1*$^{+}$ and *ccl34b.1*$^{−}$ microglia, with the color indicating *P* value. (**G** and **H**) Representative images (G) and quantification (H) of parenchymal *lck*$^{+}$ T cells in the transverse midbrain sections of WT and *E. coli*–injected *Tg(lck:DsRedx)* fish ($n = 4$) at 1 dpi. (**I**) Reverse transcription polymerase chain reaction (RT-PCR) showing the expression level of *lck* in the whole brain of *E. coli*–injected WT ($n = 3$) and *csf1ra* mutants ($n = 4$) at 1 dpi.

(e.g., *il1b* and *tnfa*), neutrophil-recruiting chemokines (e.g., *cxcl8a*, *csf3a*, and *csf3b*), and antimicrobial effectors (e.g., *acod1*, *ncf1*, and *lygl1*) (Fig. 6C), indicating that *ccl34b.1*$^{+}$ microglia might be the main effector cells to resolve the bacterial infection, which is consistent with their behavioral dynamics (Figs. 4 and 5). In contrast, the *ccl34b.1*$^{−}$ microglia up-regulated several genes in the *cxcl11* chemokine family (e.g., *cxcl11.3*, *cxcl11.7*, *cxcl11.6*, *cxcl11.1*, and *cxcl11.5*) (Fig. 6D), which have been reported to be involved in the recruitment of T cells and macrophages to the infection sites and are important for the resolution of inflammation and tissue regeneration (*30*, *31*). To explore the potential roles of these up-regulated *cxcl11* chemokines in T cell recruitment, we examined the CNS infiltration

of T cells upon bacterial infection. The number of *lck*$^+$ T cells in the *E. coli*–injected brain parenchyma slightly increased at 1 day postinjection (dpi), which was temporally correlated with up-regulation of *cxcl11* chemokines in the *ccl34b.1*$^-$ microglia (Fig. 6, G and H). To further dissect the possible roles of *ccl34b.1*$^+$ microglia and *ccl34b.1*$^-$ microglia in the T cell infiltration process, we took advantage of the *csf1ra* mutants, which are specifically deficient in *ccl34b.1*$^+$ microglia but not *ccl34b.1*$^-$ microglia (Fig. 2, F and G). *E. coli* cells were injected into the cerebroventricles of WT or *csf1ra* mutants, and whole brains were collected at 1 dpi to assay the relative expression levels of *cxcl11* chemokines and T cell marker *lck*. As expected, expression of *cxcl11* chemokines in the *E. coli*–challenged *csf1ra* mutants was up-regulated at levels similar to those of their WT counterparts (fig. S6). Expression levels of the T cell marker *lck* increased with similar fold changes in both *E. coli*–challenged WT and *csf1ra* mutants (Fig. 6I), indicating that the *ccl34b.1*$^-$ microglia play a major role in this process. Although the direct involvement of the *ccl34b.1*$^-$ microglia–derived *cxcl11* chemokines in T cell infiltration needs to be further validated, our data indicate a potential role for *ccl34b.1*$^-$ microglia in the recruitment and regulation of peripheral immune cells through releasing chemokines and immune regulators. Collectively, these results indicate that the *ccl34b.1*$^+$ and *ccl34b.1*$^-$ microglia collaboratively shape an immune response, and we designate the *ccl34b.1*$^+$ and the *ccl34b.1*$^-$ subpopulations as phagocytotic and regulatory microglia, respectively.

DISCUSSION

In this study, we have identified two distinct microglial populations throughout juvenile and adult stages in zebrafish that exhibit distinct characteristics in cellular phenotypes, development, behavior, and function. Our study provides the first solid evidence thus far of heterogeneity and functional diversification of microglia in vertebrates, adding a new dimension of complexity to the intriguing microglia field. Although several notable features have been characterized in this study, much more remains to be discovered.

One of the most urgent questions to be answered is whether similar heterogeneous microglial populations also exist in higher vertebrates, especially mammals. While recent scRNA-seq analysis in mice and other mammals has revealed that adult microglia in these species are rather homogeneous (*15*–*18*), higher heterogeneity has been found in human microglia (*17*, *19*, *20*). However, whether the reported heterogeneity of human microglia represents different states of microglia or distinct populations requires further investigation. We speculate that the resemblances between mammalian microglia and the two distinct microglial populations that we identified in zebrafish probably exist only at the phenotypic level, and not at the transcriptomic level. Another possibility to be tested is that microglial functional versatility has evolved in two different ways: either to become more adaptable (as in mammals) or to evolve functional specialization (as in zebrafish), given the fact that zebrafish have experienced multiple rounds of whole-genome duplication (*32*). Further studies, such as reinvestigation of the functional heterogeneity of mammalian microglia, identification of the key transcriptional networks that shape the cell fates of the two microglial populations in zebrafish, and comparative phylogenetic studies of the ontogeny and function of microglia of a wider array of animal species, are required to distinguish between these possibilities. In addition, several classes of brain macrophages—perivascular, meningeal, and choroid plexus macrophages—occupy distinct CNS niches and contribute importantly to CNS homeostasis, but are poorly characterized in zebrafish (*6*). Although a fraction of the *ccl34b.1*$^+$ cells were identified in the periventricular region (Fig. 5 and fig. S5), most of the *ccl34b.1*$^+$ and *ccl34b.1*$^-$ microglia reside in the parenchyma, excluding the possibility that these calls represent the different groups of brain macrophages identified in mammals. In summary, regarding the capricious functional phenotypes of microglia and their versatile roles, the clear compartmentalization within the two microglial populations in zebrafish provides a valuable model for addressing a variety of challenging questions and thus serve to complement microglial research in other species.

As reported in the results, one of the key differences between the two microglial populations in zebrafish is their morphology. The *ccl34b.1*$^+$ phagocytotic microglia are relatively amoeboid with a large soma and only a few thin protrusions, while the *ccl34b.1*$^-$ regulatory microglia exhibit a rather ramified morphology with complex protrusions. This difference is informative because the morphology of microglia is usually indicative of their functional states. For instance, during CNS development, microglia present an amoeboid morphology with higher phagocytosis capability and distinct secretory patterns for the effective removal of apoptotic neurons and inappropriately wired neural networks (*4*). As the CNS matures, microglia acquire a ramified shape, the dominant morphology of resting microglia in the adult CNS, and constantly surveil the environment by actively sending protrusions (*1*, *2*). Ramified microglia can switch back to amoeboid morphology in response to danger signals and concurrently change their secretory profiles. This activation phenotype can effectively remove invading pathogens and other insults but also exerts tissue-damaging effects if dysregulated, which is commonly seen in neuropathologies (*4*). We have shown here that the amoeboid *ccl34b.1*$^+$ phagocytotic microglia have high phagocytosis capability and mobility, while the ramified *ccl34b.1*$^-$ regulatory microglia actively remodel their protrusions; however, to what extent these cell types are equivalent to activated microglia or resting microglia remain unclear. Nonetheless, the distinct phenotypes of these microglia indicate that they may fulfill complementary functions under physiological and pathological conditions, thus offering an interesting scenario to dissect the exact contribution of each cell type and to help gain new insight into the dynamic roles of amoeboid and ramified microglia in general.

Another interesting clue comes from the distribution pattern of the two microglial populations. Distinct from the widely distributed and highly mobile *ccl34b.1*$^+$ phagocytotic microglia, *ccl34b.1*$^-$ regulatory microglia are enriched in the white matter extending from the forebrain to the hindbrain. This region harbors many of the tracts and commissures, ascending and descending projections, and the reticular formation, a most complexly wired neuronal network that reciprocally connects different brain regions and is essential for motor control and the maintenance of arousal and consciousness (*33*). The coincidence that the *ccl34b.1*$^-$ regulatory microglia are abundantly found in this region strongly indicates that these microglia may help to refine the network by regulating neurite development or myelination. The association of microglia with developing axons during development has been observed in many species (*34*–*37*), and recently, a transiently existing microglia population was found in postnatal brain regions enriched for white matter, such as the corpus callosum and cerebellum (*15*, *16*, *38*, *39*). These white matter–associated microglia express genes for the maintenance and differentiation of

neural and glial progenitors (*38*, *39*), and dysfunction or depletion of these microglia results in brain abnormalities, including defasciculation of dorsal callosal axons in the corpus callosum, defective innervation of dopamine dopaminergic axons in the forebrain, and incorrect positioning of interneurons in the cortical networks (*40*, *41*). It will be interesting to dissect the possible functions of *ccl34b.1*$^-$ regulatory microglia in the wiring of different brain regions in zebrafish.

Last, in addition to the myeloid master regulator *pu.1/spi1*, the *ccl34b.1*$^-$ regulatory microglia express considerable levels of several transcription factors (e.g., *irf8*, *id2a*, and *batf3*) essential for the development of dendritic cells (DCs) (Fig. 3), the professional antigen-presenting cells important for T cell activation (*42*). Although DCs in the teleosts remain poorly characterized, recent studies in trout have identified a CD8α$^+$ MHC II$^+$ DC-like subpopulation with phenotypical and functional features of DCs in the skin, respiratory surfaces, and intestine (*43*–*45*). These DC-like cells also expressed *irf8* and *batf3* (*43*–*45*), key transcription factors for DCs that are enriched in the *ccl34b.1*$^-$ regulatory microglia. Whether the *ccl34b.1*$^-$ regulatory microglia share the same cell lineages with peripheral DC-like cells remains an interesting question. Nonetheless, expression of the core regulatory elements of DCs strongly indicates that the *ccl34b.1*$^-$ regulatory microglia may have some functional characteristics of DCs. Consistent with this notion, the *ccl34b.1*$^-$ regulatory microglia express several genes involved in the regulation of T cells under both homeostatic and inflammatory conditions. For example, they express a high level of *ccl19a.1*, a chemokine that plays important roles in the recruitment of lymphocytes to lymphoid organs. They also express *il12ba*, whose mammalian homologous is mainly secreted by DCs and can stimulate the differentiation of T helper cells in mammals (*46*). Another possible T cell regulatory gene highly expressed in the *ccl34b.1*$^-$ regulatory microglia is *siglec15l* (sialic acid–binding immunoglobulin-like lectin 15, like), whose human ortholog has been reported to function as a critical immune suppressor for T cells (*47*). Last, the possible role of the *ccl34b.1*$^-$ regulatory microglia in the regulation of T cells is further supported by the fact that, upon acute bacterial infection, *ccl34b.1*$^-$ regulatory microglia up-regulate expression of the CXCL11 family (*cxcl11.3*, *cxcl11.7*, *cxcl11.6*, *cxcl11.1*, and *cxcl11.5*), whose mammalian ortholog has been reported to promote the infiltration of T cells, natural killer cells, and macrophages to the infection site (*30*, *31*). The potential interaction between the *ccl34b.1*$^-$ regulatory microglia and the adaptive immune system, especially T cells, remains an interesting topic to be explored.

MATERIALS AND METHODS

Study design

Sample size, replicates, and data inclusion/exclusion criteria

For all quantitative measurements in the transverse midbrain section, at least three section slices from similar midbrain position were chosen and quantified. For ratio quantification, all the signals in one section slice are counted. For density quantification, a similar quantification region was chosen for all section slices. For RNA-seq analysis, at least three biological replicates, each with at least three technological replicates, were initially set up for each group. On the basis of the quality of the complementary DNA (cDNA) library, one technological replicate was chosen from each biological replicate to proceed to RNA-seq analysis. Samples that failed in cDNA and library generation were not further processed by RNA-seq analysis. There are only two biological replicates in the ctrl (control) group for the CNS bacterial infection experiment, but we did not use the ctrl group dataset in the subsequent DE analysis.

Randomization and blinding

For all the treatment and RNA-seq analysis, randomly chosen WT or mutant fish that were raised under the same condition were used. Gender bias was prevented. Processing of RNA-seq data and clustering analysis were initially performed blinded and unblinded in the following DE analysis.

Animals

Zebrafish were maintained following a standard protocol (*48*). In summary, zebrafish were kept at 28.5°C with 14-hour light and 10-hour dark cycle. Embryos were collected after natural spawning and kept in 0.5× E2 medium containing methylene blue (egg water) with or without 0.003% *N*-phenylthiourea (P7629, Sigma-Aldrich) to avoid pigmentation. All animal experiments were performed under approval from the Hong Kong University of Science and Technology's Animal Studies Committee.

ABSR WT, *csf1ra*^{j4e1} (*49*), *Tg(coro1a:DsRedx)* (*50*), *Tg(hsp70:mCherry-T2a-CreERT2)* (*51*), *Tg(mpeg1:DsRedx)* short for *Tg(mpeg1:loxP-DsRedx-loxP-GFP)* (*52*), *Tg(lck:DsRedx)* short for *Tg(lck:loxP-DsRedx-loxP-GFP)* (*53*), and *TgBAC(ccl34b.1:eGFP)*^{hkz035Tg} are used in this study. The developmental stages of zebrafish were indicated in the figure legends.

BAC transgenesis

The generation of the BAC transgenic line *TgBAC(ccl34b.1:eGFP)* was performed following a previous study (*54*). BAC clone CH211-47 k13 containing *ccl34b.1* was chosen and purchased from CHORI-211 library. The pCR8GW-iTol2amp and pBSSK(+)-GFP-FRT-Kan-FRT constructs were requested from K. Kawakami's laboratory. The pSIM29 construct was requested from D. L. Court's laboratory. The pSIM29 construct, which contains a heat-inducible λ-Red recombination system and hygromycin resistance, was further engineered by inserting an arabinose-inducible flippase (FLP) gene, generating the pSIM29-FLP construct. The pSIM29-FLP construct was electroporated into the DH10B strain containing the BAC clone CH211-47 k13. In the first round of recombination, an *iTol2* cassette, which consists of the inverted L200 and R150 of the *Tol2* transposon flanking an ampicillin resistance gene, was polymerase chain reaction (PCR)–amplified with primers containing 50–base pair (bp) homologous arms that are homologous to the backbone of the BAC plasmid. The *iTol2* cassette with homologous arms was then electroporated into the DH10B-pSIM29-FLP-CH211-47 K13, and the successfully recombined clone was selected by ampicillin resistance. In the second round of recombination, a GFP-FRT-Kan-FRT (flippase recognition target) reporter cassette, which consists of the GFP and FRT-flanked kanamycin resistance gene, was cloned into a construct containing two 1-kb homologous arms of the *ccl34b.1* locus. This construct was then used as the template for the PCR amplification of the GFP-FRT-Kan-FRT reporter cassette with *ccl34b.1* homologous arm, and the PCR product was electroporated into the DH10B-*iTol2*-pSIM29-FLP-CH211-47 K13, followed by kanamycin resistance selection. Last, the FRT-flanked kanamycin resistance gene was removed by inducing the expression of FLP with arabinose. The final BAC, CH211-47 K13-*iTol2*-GFP, was extracted from the DH10B using the Nucleobond BAC 100 Kit (740579, Macherey-Nagel). The BAC (30 ng/μl) and transposase mRNA (50 ng/μl) were injected into one-cell-stage WT embryos. The injected embryos were raised to adults and outcrossed with WT for transgenic screening.

Cryo-section and immunofluorescent antibody staining

Juvenile fish (20 dpf, 1 month old, 40 dpf, 2 months old) were anesthetized on ice and fixed in 4% paraformaldehyde (PFA) at 4°C for 1 day. Adult fish were anesthetized on ice, and their brains were freshly dissected and fixed in 4% PFA at 4°C for 1 day. After washing with PBS, fixed samples were dehydrated with 30% sucrose in PBS at 4°C for 1 day, then soaked in coagulating solution (1.5% agar + 5% sucrose), and subjected to cryo-section at 30-μm thickness. Slides were dried overnight.

Fluorescent immunostaining on section samples was performed as previously described (*55*). Samples were incubated sequentially with (i) blocking buffer [5% fetal bovine serum (FBS) in PBS] at room temperature for 1 hour, (ii) primary antibodies (1:400 dilution in blocking buffer) at room temperature for 1 hour, and (iii) secondary antibodies (1:400 dilution in blocking buffer) at room temperature for 1 hour. Primary antibodies used in this study are rabbit anti-DsRed antibody (632496, Clontech), goat anti-GFP antibody (ab6658, Abcam), and rabbit anti-Lcp1 antibody (*56*). Secondary antibodies used in this study are Alexa Fluor 555 anti-rabbit antibody (A31572, Invitrogen) and Alexa Fluor 488 anti-goat antibody (A11055, Invitrogen). Section samples were sealed with cover slides and imaged using a Leica SP8 confocal microscope.

Fluorescent in situ hybridization and immunostaining

Antisense digoxigenin-labeled RNA probes of *ccl34b.1* were synthesized in vitro. WISH (whole-mount in situ hybridization) was performed following a previous study (*57*). Adult brains were mounted in 3% agarose and cut into thick slices using a blade. Embryos were anesthetized on ice. All samples were then fixed in 4% PFA and permeabilized with 100% methanol. After rehydration, samples were furthered permeabilized using proteinase K (P8107S, New England Biolabs; 1:2000 dilution in PBS), refixed with 4% PFA, and prehybridized in hybridization buffer [50% formamide, 1 M citric acid, 0.1% Tween 20, heparin (50 μg/ml), transfer RNA (500 μg/ml), and 5× SSC (saline-sodium citrate)]. Samples were then changed to the hybridization buffer containing RNA probe (0.5 to 1 ng/μl) and incubated at 67°C overnight. The next day, samples were applied to a series of stringent washing using different concentrations of SSC buffer, incubated in the blocking buffer at room temperature for 1 hour, and then with anti–digoxigenin-horseradish peroxidase (11207733910, Roche; 1:2000 dilution in blocking buffer). After washing with PBS, samples were stained with TSA (tyramide signal amplification) Plus Cyanine 3 System (NEL744001KT, PerkinElmer).

After confirming the fluorescent signal, samples were processed to subsequent immunostaining. Samples were incubated in blocking buffer for 1 hour, primary antibody (1:400 dilution in blocking buffer) for overnight, PBS multiples times, and secondary antibody (1:400 dilution in blocking buffer) for overnight. Primary antibodies used in this study are rabbit anti-DsRed antibody (632496, Clontech), goat anti-GFP antibody (ab6658, Abcam), and rabbit anti-Lcp1 antibody (*56*). Secondary antibodies used in this study are Alexa Fluor 555 anti-rabbit antibody (A31572, Invitrogen) and Alexa Fluor 488 anti-goat antibody (A11055, Invitrogen). Fluorescent images were captured using a Leica SP8 confocal microscope.

Infrared-mediated temporal-spatial resolution cell labeling

Experiments were performed according to the previous report (*26*). A 1345-nm infrared (IR) laser was focused on specific regions of embryos, which were anesthetized with 0.01% Tricaine (A5040, Sigma-Aldrich) and mounted in methylcellulose. The RBI and the AGM region of zebrafish embryos were heat-shocked at 230 mW in three positions or a single position with 30 s per hit. The heat-shocked embryos were incubated with 5 μM (Z)-4-hydroxytamoxifen (H7904, Sigma-Aldrich) for 24 hours and then changed back into fresh egg water and raised to the desired stage.

Isolation of microglia by FACS

Briefly, *TgBAC(ccl34b.1:eGFP) Tg(mpeg1:DsRedx)* fish were anesthetized on ice, and brains were freshly dissected and homogenized with needle and syringe in ice-cold PBS. After a brief wash and centrifugation, the homogenates were resuspended in 0.25% trypsin-EDTA (T4049, Sigma-Aldrich) and incubated at 30°C for 20 to 30 min. After termination of the reaction with 10 μM $CaCl_2$ and 10% FBS, samples were centrifuged and washed with ice-cold 1% bovine serum albumin/PBS buffer, and lastly pushed through a Falcon 40-μm Cell Strainer (352340, BD Falcon) to obtain single-cell suspensions. $ccl34b.1^{+}mpeg1^{+}$ and $ccl34b.1^{-}mpeg1^{+}$ microglia (100 cells for each sample) were directly sorted into lysis buffer (0.2% Triton X-100 solution) in a FACSAria III sorter (BD Biosciences) based on the eGFP and DsRedx fluorescence.

cDNA preparation and bulk RNA-seq

The Smart-seq2 protocol was used for whole-transcriptome amplification and library preparation (*58*, *59*). Cell lysates were hybridized together with oligo(dT) primer and deoxynucleotide triphosphate (U1515, Promega) at 72°C for 3 min and then added with reverse transcription mix containing SuperScript II Reverse Transcriptase (18064014, Invitrogen) and a template-switching oligo. After reverse transcription, first-strand reaction products were PCR-amplified using KAPA HiFi HotStart ReadyMix (KK2602, KAPA) with 24 PCR cycles and purified using Ampure XP beads (A63881, Beckman Coulter) with a magnetic stand. cDNA quality was assessed using the Agilent Fragment Analyzer System.

Sequencing libraries were prepared using the TruePrep DNA Library Prep Kit V2 for Illumina (TD503, Vazyme) following the instructions (0.5 ng of cDNA input). After tagmentation, samples were amplified with the TruePrep Index Kit V2 for Illumina (TD202, Vazyme; 12 cycles) and purified with the Ampure XP beads (A63881, Beckman Coulter). Library quality was assessed using the Agilent Fragment Analyzer System. For the samples from the WT fish in result 3, NextSeq sequencing was performed to an average depth of 2.2×10^7 raw reads per sample. Samples from the *E. coli* injection experiments in result 5 were sent to Novogene for Illumina Hiseq X Ten 150-bp paired-end sequencing with an average depth of 4.2×10^6 raw reads per sample.

Bioinformatic analysis of bulk sequencing

Reads were aligned to the GRCz11.94 (danRer11) zebrafish reference genome using STAR. Aligned reads were converted to counts for each gene using featureCounts. Quality control, filtering of lowly expressed genes, normalization, transformation, and DE gene analysis, was performed using the pipeline of the DESeq2 package. The counts were processed through a variance stabilizing transformation procedure in the DESeq2 package to obtain transformed values and based on which PCA was performed. Pairwise comparisons were performed using the DESeq2 package, with a cutoff of adjusted $P < 0.05$, $|\text{fold-change}| > 2$. Heatmaps with hierarchical clustering were made using the heatmap.2 package with the transformed values in which the expression of each gene was scaled across all samples (z-scored). GO term enrichment analysis was performed with the GO molecular functions sources and the GO biological processes sources in the Metascape website (*60*). Enriched terms ($P < 0.01$, a minimum count of 3, and an enrichment factor of >1.5) were grouped into clusters based on their membership similarities and visualized in a network

plot using Cytoscape in which node color indicates *P* value, node size indicates membership size, and the connecting edges indicates their membership similarities.

Acute brain slice culture, time-lapse imaging, and cell tracing

Fish were anesthetized on ice, and their brains were freshly dissected and mounted in 3% low-melting agarose in PBS. After the agarose solidified, the agarose blocks were sectioned using a Leica VT1200 S vibrating blade microtome (thickness, 200 μm; speed, 0.08; vibration, 0.5). Slices were immediately collected into ice-cold PBS and subsequently transferred into a Millicell culture insert (PICM01250, Millipore) in a glass-bottom imaging dish with 300 μl of Leibovitz's L-15 medium (11415064, Gibco) containing 10% FBS and imaged on a Leica SP8 confocal microscope with a 28°C thermal chamber. Time-lapse imaging was carried out with a time interval of 1 to 2 min. The imaging file was processed with ImageJ software, and cell tracking analysis was performed using the MTrackJ plugin.

Phagocytosis assay

For the phagocytosis assay in the acute brain slice culture, brain slices were prepared as previously described and incubated with pHrodo Red *E. coli* BioParticles Conjugate for Phagocytosis (0.25 mg/ml; P35361, Invitrogen) or pHrodo Green *E. coli* BioParticles Conjugate for Phagocytosis (P35366, Invitrogen) in the Leibovitz's L-15 medium (11415064, Gibco) containing 10% FBS.

For the phagocytosis assay in cell suspensions, microglia suspensions were prepared as previously described and incubated with pHrodo Red *E. coli* BioParticles Conjugate for Phagocytosis (0.8 mg/ml; P35361, Invitrogen) in the Leibovitz's L-15 medium (11415064, Gibco) containing 10% FBS for 1 hour at 30°C. After incubation, cell suspensions were analyzed in a FACSAria III sorter (BD Biosciences).

Cerebroventricular microinjection of E. coli into the brain

The cerebroventricular microinjection was performed according to a previous report (*61*). Briefly, fish were anesthetized with 0.01% Tricaine (A5040, Sigma-Aldrich), and incisions were made on the skull using a 27-gauge needle. A glass capillary was then inserted into the incision, and around 8 nl of PBS or *E. coli* (optical density at 600 nm = 1 in PBS), together with Alexa Fluor 647 Hydrazide (A20502, Invitrogen), was injected into the brain. The fluorescence of Alexa Fluor 647 in the brain was monitored to confirm the injection was successful. Fish were then raised to the desired stages.

RNA extraction, cDNA synthesis, and RT-PCR

Fish were anesthetized on ice, and brains were freshly dissected and homogenized in Buffer RLT (RNeasy Mini Kit) with needles and syringes. The RNA was extracted by an RNeasy Mini Kit (74104, QIAGEN) and reverse-transcribed with SuperScript IV VILO Master Mix (11756050, Invitrogen). Real-time PCR was performed to examine the transcripts corresponding to the coding region of *cxcl11.1*, *cxcl11.3*, *cxcl11.5*, *cxcl11.6*, *cxcl11.7*, and *lck*. Primers for reverse transcription PCR (RT-PCR) are listed as follows: *cxcl11.1*, 5′-TCGAAAGTGGTTTAGGGTGG-3′ (forward) and 5′-ATGTCCACAGGATGGACTTG-3′ (reverse); *cxcl11.5*, 5′-ATTACGGCTTCAAACAGTCA-3′ (forward) and 5′-CCACAAGATGGACTTGGATG-3′ (reverse); *cxcl11.3/6/7*, 5′-CTGAAAAACGGTGCAGGACA-3′ (forward) and 5′-AAGGCAGTCGGTGCTGATGT-3′ (reverse); *lck*, 5′-GAACAGCATGGAGACAGAACC-3′ (forward) and 5′-CATCAAGCACTACAGGATCCG-3′ (reverse).

Quantification and statistical analysis

Statistical parameters including the exact value of *n* are reported in the figures and figure legends. All values represent means with SD. Statistical significance is shown as follows: ns, $P>0.05$; $*P \leq 0.05$; $***P \leq 0.001$; and $****P \leq 0.0001$. All statistical analyses were performed using GraphPad Prism version 8. Unpaired Student's *t* tests were used to calculate the *P* value for pairwise comparisons. For multiple comparisons, significances were calculated using two-way analysis of variance (ANOVA), followed by Sidak's multiple comparisons test or Tukey's multiple comparisons test. Two-tailed *P* values are used for all *t* tests.

SUPPLEMENTARY MATERIALS

Supplementary material for this article is available at http://advances.sciencemag.org/cgi/content/full/6/47/eabd1160/DC1

REFERENCES AND NOTES

1. A. Nimmerjahn, F. Kirchhoff, F. Helmchen, Resting microglial cells are highly dynamic surveillants of brain parenchyma in vivo. *Science* **308**, 1314–1318 (2005).
2. D. Davalos, J. Grutzendler, G. Yang, J. V. Kim, Y. Zuo, S. Jung, D. R. Littman, M. L. Dustin, W.-B. Gan, ATP mediates rapid microglial response to local brain injury in vivo. *Nat. Neurosci.* **8**, 752–758 (2005).
3. U.-K. Hanisch, H. Kettenmann, Microglia: Active sensor and versatile effector cells in the normal and pathologic brain. *Nat. Neurosci.* **10**, 1387–1394 (2007).
4. R. M. Ransohoff, V. H. Perry, Microglial physiology: Unique stimuli, specialized responses. *Annu. Rev. Immunol.* **27**, 119–145 (2009).
5. M. Prinz, J. Priller, Microglia and brain macrophages in the molecular age: From origin to neuropsychiatric disease. *Nat. Rev. Neurosci.* **15**, 300–312 (2014).
6. Q. Li, B. A. Barres, Microglia and macrophages in brain homeostasis and disease. *Nat. Rev. Immunol.* **18**, 225–242 (2018).
7. L. J. Lawson, V. H. Perry, P. Dri, S. Gordon, Heterogeneity in the distribution and morphology of microglia in the normal adult mouse brain. *Neuroscience* **39**, 151–170 (1990).
8. S. Elkabes, E. M. DiCicco-Bloom, I. B. Black, Brain microglia/macrophages express neurotrophins that selectively regulate microglial proliferation and function. *J. Neurosci.* **16**, 2508–2521 (1996).
9. L.-q. Ren, B. Lubrich, K. Biber, P. J. Gebicke-Haerter, Differential expression of inflammatory mediators in rat microglia cultured from different brain regions. *Brain Res. Mol. Brain Res.* **65**, 198–205 (1999).
10. K. Grabert, T. Michoel, M. H. Karavolos, S. Clohisey, J. K. Baillie, M. P. Stevens, T. C. Freeman, K. M. Summers, B. W. McColl, Microglial brain region-dependent diversity and selective regional sensitivities to aging. *Nat. Neurosci.* **19**, 504–516 (2016).
11. P. Ayata, A. Badimon, H. J. Strasburger, M. K. Duff, S. E. Montgomery, Y.-H. E. Loh, A. Ebert, A. A. Pimenova, B. R. Ramirez, A. T. Chan, J. M. Sullivan, I. Purushothaman, J. R. Scarpa, A. M. Goate, M. Busslinger, L. Shen, B. Losic, A. Schaefer, Epigenetic regulation of brain region-specific microglia clearance activity. *Nat. Neurosci.* **21**, 1049–1060 (2018).
12. F. Ginhoux, M. Greter, M. Leboeuf, S. Nandi, P. See, S. Gokhan, M. F. Mehler, S. J. Conway, L. G. Ng, E. R. Stanley, I. M. Samokhvalov, M. Merad, Fate mapping analysis reveals that adult microglia derive from primitive macrophages. *Science* **330**, 841–845 (2010).
13. A. Mildner, H. Schmidt, M. Nitsche, D. Merkler, U.-K. Hanisch, M. Mack, M. Heikenwalder, W. Brück, J. Priller, M. Prinz, Microglia in the adult brain arise from Ly-6C^{hi}CCR2^{+} monocytes only under defined host conditions. *Nat. Neurosci.* **10**, 1544–1553 (2007).
14. B. Ajami, J. L. Bennett, C. Krieger, W. Tetzlaff, F. M. V. Rossi, Local self-renewal can sustain CNS microglia maintenance and function throughout adult life. *Nat. Neurosci.* **10**, 1538–1543 (2007).
15. Q. Li, Z. Cheng, L. Zhou, S. Darmanis, N. F. Neff, J. Okamoto, G. Gulati, M. L. Bennett, L. O. Sun, L. E. Clarke, J. Marschallinger, G. Yu, S. R. Quake, T. Wyss-Coray, B. A. Barres, Developmental heterogeneity of microglia and brain myeloid cells revealed by deep single-cell RNA sequencing. *Neuron* **101**, 207–223.e10 (2018).
16. T. R. Hammond, C. Dufort, L. Dissing-Olesen, S. Giera, A. Young, A. Wysoker, A. J. Walker, F. Gergits, M. Segel, J. Nemesh, S. E. Marsh, A. Saunders, E. Macosko, F. Ginhoux, J. Chen, R. J. M. Franklin, X. Piao, S. A. McCarroll, B. Stevens, Single-cell RNA sequencing of microglia throughout the mouse lifespan and in the injured brain reveals complex cell-state changes. *Immunity* **50**, 253–271.e6 (2019).
17. T. Masuda, R. Sankowski, O. Staszewski, C. Böttcher, L. Amann, C. Scheiwe, S. Nessler, P. Kunz, G. van Loo, V. A. Coenen, P. C. Reinacher, A. Michel, U. Sure, R. Gold, D. Grün, J. Priller, C. Stadelmann, M. Prinz, Spatial and temporal heterogeneity of mouse and human microglia at single-cell resolution. *Nature* **566**, 388–392 (2019).
18. L. Geirsdottir, E. David, H. Keren-Shaul, A. Weiner, S. C. Bohlen, J. Neuber, A. Balic, A. Giladi, F. Sheban, C.-A. Dutertre, C. Pfeifle, F. Peri, A. Raffo-Romero, J. Vizioli,

K. Matiasek, C. Scheiwe, S. Meckel, K. Mätz-Rensing, F. van der Meer, F. R. Thormodsson, C. Stadelmann, N. Zilkha, T. Kimchi, F. Ginhoux, I. Ulitsky, D. Erny, I. Amit, M. Prinz, Cross-species single-cell analysis reveals divergence of the primate microglia program. *Cell* **179**, 1609–1622.e16 (2019).
19. C. Böttcher, S. Schlickeiser, M. A. M. Sneeboer, D. Kunkel, A. Knop, E. Paza, P. Fidzinski, L. Kraus, G. J. L. Snijders, R. S. Kahn, A. R. Schulz, H. E. Mei; NBB-Psy, E. M. Hol, B. Siegmund, R. Glauben, E. J. Spruth, L. D. de Witte, J. Priller, Human microglia regional heterogeneity and phenotypes determined by multiplexed single-cell mass cytometry. *Nat. Neurosci.* **22**, 78–90 (2018).
20. R. Sankowski, C. Böttcher, T. Masuda, L. Geirsdottir, Sagar, E. Sindram, T. Seredenina, A. Muhs, C. Scheiwe, M. J. Shah, D. H. Heiland, O. Schnell, D. Grün, J. Priller, M. Prinz, Mapping microglia states in the human brain through the integration of high-dimensional techniques. *Nat. Neurosci.* **22**, 2098–2110 (2019).
21. N. Oosterhof, I. R. Holtman, L. E. Kuil, H. C. van der Linde, E. W. G. M. Boddeke, B. J. L. Eggen, T. J. van Ham, Identification of a conserved and acute neurodegeneration-specific microglial transcriptome in the zebrafish. *Glia* **65**, 138–149 (2017).
22. F. Peri, C. Nüsslein-Volhard, Live imaging of neuronal degradation by microglia reveals a role for v0-ATPase a1 in phagosomal fusion in vivo. *Cell* **133**, 916–927 (2008).
23. D. Sieger, C. Moritz, T. Ziegenhals, S. Prykhozhij, F. Peri, Long-range Ca^{2+} waves transmit brain-damage signals to microglia. *Dev. Cell* **22**, 1138–1148 (2012).
24. F. Mazaheri, O. Breus, S. Durdu, P. Haas, J. Wittbrodt, D. Gilmour, F. Peri, Distinct roles for BAI1 and TIM-4 in the engulfment of dying neurons by microglia. *Nat. Commun.* **5**, 4046 (2014).
25. Y. Li, X.-F. Du, C.-S. Liu, Z.-L. Wen, J.-L. Du, Reciprocal regulation between resting microglial dynamics and neuronal activity in vivo. *Dev. Cell* **23**, 1189–1202 (2012).
26. J. Xu, L. Zhu, S. He, Y. Wu, W. Jin, T. Yu, J. Y. Qu, Z. Wen, Temporal-spatial resolution fate mapping reveals distinct origins for embryonic and adult microglia in zebrafish. *Dev. Cell* **34**, 632–641 (2015).
27. S. Wu, R. Xue, S. Hassan, T. M. L. Nguyen, T. Wang, H. Pan, J. Xu, Q. Liu, W. Zhang, Z. Wen, Il34-Csf1r pathway regulates the migration and colonization of microglial precursors. *Dev. Cell* **46**, 552–563.e4 (2018).
28. F. Ellett, L. Pase, J. W. Hayman, A. Andrianopoulos, G. J. Lieschke, *mpeg1* promoter transgenes direct macrophage-lineage expression in zebrafish. *Blood* **117**, e49–e56 (2011).
29. X. Lin, Q. Zhou, C. Zhao, G. Lin, J. Xu, Z. Wen, An ectoderm-derived myeloid-like cell population functions as antigen transporters for langerhans cells in zebrafish epidermis. *Dev. Cell* **49**, 605–617.e5 (2019).
30. K. E. Cole, C. A. Strick, T. J. Paradis, K. T. Ogborne, M. Loetscher, R. P. Gladue, W. Lin, J. G. Boyd, B. Moser, D. E. Wood, B. G. Sahagan, K. Neote, Interferon–inducible T cell alpha chemoattractant (I-TAC): A novel non-ELR CXC chemokine with potent activity on activated T cells through selective high affinity binding to CXCR3. *J. Exp. Med.* **187**, 2009–2021 (1998).
31. V. Torraca, C. Cui, R. Boland, J.-P. Bebelman, A. M. van der Sar, M. J. Smit, M. Siderius, H. P. Spaink, A. H. Meijer, The CXCR3-CXCL11 signaling axis mediates macrophage recruitment and dissemination of mycobacterial infection. *Dis. Model. Mech.* **8**, 253–269 (2015).
32. S. M. K. Glasauer, S. C. F. Neuhauss, Whole-genome duplication in teleost fishes and its evolutionary consequences. *Mol. Genet. Genomics* **289**, 1045–1060 (2014).
33. M. F. Wullimann, B. Rupp, H. Reichert, *Neuroanatomy of the Zebrafish Brain* (Birkhäuser Basel, 1996).
34. M. A. Cuadros, C. Martin, P. Coltey, A. Almendros, J. Navascués, First appearance, distribution, and origin of macrophages in the early development of the avian central nervous system. *J. Comp. Neurol.* **330**, 113–129 (1993).
35. I. Dalmau, B. Finsen, N. Tønder, J. Zimmer, B. González, B. Castellano, Development of microglia in the prenatal rat hippocampus. *J. Comp. Neurol.* **377**, 70–84 (1997).
36. I. Dalmau, B. Finsen, J. Zimmer, B. González, B. Castellano, Development of microglia in the postnatal rat hippocampus. *Hippocampus* **8**, 458–474 (1998).
37. C. Verney, A. Monier, C. Fallet-Bianco, P. Gressens, Early microglial colonization of the human forebrain and possible involvement in periventricular white-matter injury of preterm infants. *J. Anat.* **217**, 436–448 (2010).
38. N. Hagemeyer, K.-M. Hanft, M.-A. Akriditou, N. Unger, E. S. Park, E. R. Stanley, O. Staszewski, L. Dimou, M. Prinz, Microglia contribute to normal myelinogenesis and to oligodendrocyte progenitor maintenance during adulthood. *Acta Neuropathol.* **134**, 441–458 (2017).
39. A. Wlodarczyk, I. R. Holtman, M. Krueger, N. Yogev, J. Bruttger, R. Khorooshi, A. Benmamar-Badel, J. J. de Boer-Bergsma, N. A. Martin, K. Karram, I. Kramer, E. W. Boddeke, A. Waisman, B. J. Eggen, T. Owens, A novel microglial subset plays a key role in myelinogenesis in developing brain. *EMBO J.* **36**, 3292–3308 (2017).
40. L. Pont-Lezica, W. Beumer, S. Colasse, H. Drexhage, M. Versnel, A. Bessis, Microglia shape corpus callosum axon tract fasciculation: Functional impact of prenatal inflammation. *Eur. J. Neurosci.* **39**, 1551–1557 (2014).
41. P. Squarzoni, G. Oller, G. Hoeffel, L. Pont-Lezica, P. Rostaing, D. Low, A. Bessis, F. Ginhoux, S. Garel, Microglia modulate wiring of the embryonic forebrain. *Cell Rep.* **8**, 1271–1279 (2014).
42. T. L. Murphy, G. E. Grajales-Reyes, X. Wu, R. Tussiwand, C. G. Briseño, A. Iwata, N. M. Kretzer, V. Durai, K. M. Murphy, Transcriptional control of dendritic cell development. *Annu. Rev. Immunol.* **34**, 93–119 (2016).
43. A. G. Granja, E. Leal, J. Pignatelli, R. Castro, B. Abós, G. Kato, U. Fischer, C. Tafalla, Identification of teleost skin $CD8\alpha^+$ dendritic-like cells, representing a potential common ancestor for mammalian cross-presenting dendritic cells. *J. Immunol.* **195**, 1825–1837 (2015).
44. I. Soleto, U. Fischer, C. Tafalla, A. G. Granja, Identification of a potential common ancestor for mammalian cross-presenting dendritic cells in teleost respiratory surfaces. *Front. Immunol.* **9**, 59 (2018).
45. I. Soleto, A. G. Granja, R. Simón, E. Morel, P. Díaz-Rosales, C. Tafalla, Identification of $CD8\alpha^+$ dendritic cells in rainbow trout (*Oncorhynchus mykiss*) intestine. *Fish Shellfish Immunol.* **89**, 309–318 (2019).
46. C. Reis e Sousa, S. Hieny, T. Scharton-Kersten, D. Jankovic, H. Charest, R. N. Germain, A. Sher, In vivo microbial stimulation induces rapid CD40 ligand–independent production of interleukin 12 by dendritic cells and their redistribution to T cell areas. *J. Exp. Med.* **186**, 1819–1829 (1997).
47. J. Wang, J. Sun, L. N. Liu, D. B. Flies, X. Nie, M. Toki, J. Zhang, C. Song, M. Zarr, X. Zhou, X. Han, K. A. Archer, T. O'Neill, R. S. Herbst, A. N. Boto, M. F. Sanmamed, S. Langermann, D. L. Rimm, L. Chen, Siglec-15 as an immune suppressor and potential target for normalization cancer immunotherapy. *Nat. Med.* **25**, 656–666 (2019).
48. M. Westerfield, *The Zebrafish Book: A Guide for The Laboratory Use of Zebrafish* (*Danio rerio*) (University of Oregon Press, 2000), vol. 385.
49. D. M. Parichy, D. G. Ransom, B. Paw, L. I. Zon, S. L. Johnson, An orthologue of the kit-related gene fms is required for development of neural crest-derived xanthophores and a subpopulation of adult melanocytes in the zebrafish, *Danio rerio*. *Development* **127**, 3031–3044 (2000).
50. J. Xu, T. Wang, Y. Wu, W. Jin, Z. Wen, Microglia colonization of developing zebrafish midbrain is promoted by apoptotic neuron and lysophosphatidylcholine. *Dev. Cell* **38**, 214–222 (2016).
51. S. Hans, D. Freudenreich, M. Geffarth, J. Kaslin, A. Machate, M. Brand, Generation of a non-leaky heat shock-inducible Cre line for conditional Cre/lox strategies in zebrafish. *Dev. Dyn.* **240**, 108–115 (2011).
52. S. He, J. Chen, Y. Jiang, Y. Wu, L. Zhu, W. Jin, C. Zhao, T. Yu, T. Wang, S. Wu, X. Lin, J. Y. Qu, Z. Wen, W. Zhang, J. Xu, Adult zebrafish Langerhans cells arise from hematopoietic stem/progenitor cells. *Elife* **7**, e36131 (2018).
53. Y. Tian, J. Xu, S. Feng, S. He, S. Zhao, L. Zhu, W. Jin, Y. Dai, L. Luo, J. Y. Qu, Z. Wen, The first wave of T lymphopoiesis in zebrafish arises from aorta endothelium independent of hematopoietic stem cells. *J. Exp. Med.* **214**, 3347–3360 (2017).
54. M. L. Suster, G. Abe, A. Schouw, K. Kawakami, Transposon-mediated BAC transgenesis in zebrafish. *Nat. Protoc.* **6**, 1998–2021 (2011).
55. T. Wendl, K. Lun, M. Mione, J. Favor, M. Brand, S. W. Wilson, K. B. Rohr, *pax2.1* is required for the development of thyroid follicles in zebrafish. *Development* **129**, 3751–3760 (2002).
56. H. Jin, R. Sood, J. Xu, F. Zhen, M. A. English, P. P. Liu, Z. Wen, Definitive hematopoietic stem/progenitor cells manifest distinct differentiation output in the zebrafish VDA and PBI. *Development* **136**, 647–654 (2009).
57. C. Thisse, B. Thisse, High-resolution in situ hybridization to whole-mount zebrafish embryos. *Nat. Protoc.* **3**, 59–69 (2008).
58. S. Picelli, O. R. Faridani, Å. K. Björklund, G. Winberg, S. Sagasser, R. Sandberg, Full-length RNA-seq from single cells using Smart-seq2. *Nat. Protoc.* **9**, 171–181 (2014).
59. S. Picelli, Å. K. Björklund, O. R. Faridani, S. Sagasser, G. Winberg, R. Sandberg, Smart-seq2 for sensitive full-length transcriptome profiling in single cells. *Nat. Methods* **10**, 1096–1098 (2013).
60. Y. Zhou, B. Zhou, L. Pache, M. Chang, A. H. Khodabakhshi, O. Tanaseichuk, C. Benner, S. K. Chanda, Metascape provides a biologist-oriented resource for the analysis of systems-level datasets. *Nat. Commun.* **10**, 1523 (2019).
61. C. Kizil, M. Brand, Cerebroventricular microinjection (CVMI) into adult zebrafish brain is an efficient misexpression method for forebrain ventricular cells. *PLOS ONE* **6**, e27395 (2011).

Acknowledgments: We thank D. Parichy (University of Virginia) for sharing the *panther*^{j4e1} mutants, M. Brand (Technische Universität Dresden) for sharing the *Tg(hsp70:mCherry-T2a-CreERT2)* line, K. Kawakami (National Institute of Genetics) and D. L. Court (National Cancer Institute) for sharing plasmids related to BAC transgenesis, D. S. He and J. Y. Qu (Hong Kong University of Science and Technology) for technical support in the IR laser system, Y. Li and J. He (Institute of Neuroscience, Chinese Academy of Sciences) for advice in BAC transgenesis, G. Wang and Z. Wu (Hong Kong University of Science and Technology) for help in RNA-seq, C. Yang and K. Liu (Hong Kong University of Science and Technology) for support in the Leica VT1200 S vibrating blade microtome, and Q. Zhou for help in bioinformatic analysis. **Funding:**

This work was supported by the National Key Research and Development Program of China (2018YFA0800200), the Research Grants Council of Hong Kong (16131916, 16102617, 16103718, C6002-17GF, N_HKUST621/17, AoE/M-09/12, and T13-605/18-W), and the Innovation and Technology Commission of Hong Kong (ITCPD/17-9). **Author contributions:** S.W. designed the work, performed the experiments, analyzed the data, and wrote the manuscript. L.T.M.N. performed the experiments and analyzed the data. H.P., S.H., and Y.D. performed the experiments. J.X. designed the work. Z.W designed the work, interpreted the data, and wrote the manuscript. **Competing interests:** The authors declare that they have no competing interests. **Data and materials availability:** The RNA-seq data are deposited in the Gene Expression Omnibus under the accession no. GSE156158. All data needed to evaluate the conclusions in the paper are present in the paper and/or the Supplementary Materials. Additional data related to this paper may be requested from the authors.

Submitted 2 June 2020
Accepted 2 October 2020
Published 18 November 2020
10.1126/sciadv.abd1160

Citation: S. Wu, L. T. M. Nguyen, H. Pan, S. Hassan, Y. Dai, J. Xu, Z. Wen, Two phenotypically and functionally distinct microglial populations in adult zebrafish. *Sci. Adv.* **6**, eabd1160 (2020).